

Understanding irradiation-induced nanoprecipitation in zirconium alloys using parallel TEM and APT

A. Harte^{a,*}, R. Prasath Babu^a, C.A. Hirst^b, T.L. Martin^b, P.A.J. Bagot^b, M.P. Moody^b, P. Frankel^a, J. Romero^c, L. Hallstadius^d, E.C. Darby^e, M. Preuss^a

^a School of Materials, The University of Manchester, Oxford Road, Manchester, M13 9PL, United Kingdom

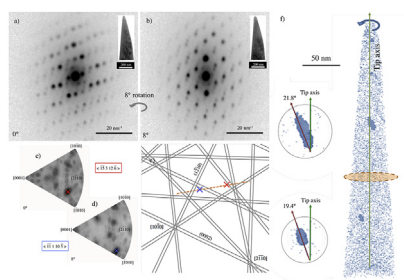
^b Department of Materials, The University of Oxford, Parks Road, Oxford, OX1 3PH, United Kingdom

^c Westinghouse Electric Company, Columbia, SC, United States

^d Westinghouse Electric Sweden AB, SE.72163, Västerås, Sweden

^e Rolls Royce Plc, Nuclear Materials, Derby, UK

GRAPHICAL ABSTRACT



ARTICLE INFO

Article history:

Received 6 April 2018

Received in revised form

13 August 2018

Accepted 15 August 2018

Available online 17 August 2018

Keywords:

Nano precipitation

Transmission electron microscopy

Atom probe tomography

Zirconium

Irradiation

ABSTRACT

We investigate nano-scale irradiation-induced precipitation in a Zr–Sn–Fe–Cr–Ni-alloy (Zircaloy-2) by combining atom probe tomography (APT) for chemical detail with scanning transmission electron microscopy (STEM) and high resolution energy dispersive X-ray (EDX) spectroscopy for wider context and complementary and correlative TEM diffraction techniques for crystallographic relationships. We find that Fe- and Cr-rich nano-rods precipitate in Zircaloy-2 following proton irradiation at 350 °C to a low dose of ~2 dpa. The long-axis of the nano-rods are aligned in a direction 12–15° from the Zr matrix (0001), align in the basal plane and are of width 1.5–5 nm. Smaller rods are of APT-determined composition $\text{Zr}_4(\text{Fe}_{0.67}\text{Cr}_{0.33})$, tending towards $\text{Zr}_3(\text{Fe}_{0.69}\text{Cr}_{0.31})$ as the rod volume increases to > 400 nm³, in agreement with STEM-EDX determination of composition resembling that of Zr_3Fe with Cr replacing some of the Fe. The Fe/Cr ratio has been shown to increase with distance from the nearest partially-dissolved $\text{Zr}(\text{Fe,Cr})_2$ phase particle. The nucleation of nano rods has implications for macroscopic irradiation-induced deformation phenomena, irradiation-induced hardening and the evolution of dislocation loops and other defects.

© 2019 The Authors. Published by Elsevier B.V. This is an open access article under the CC BY license (<http://creativecommons.org/licenses/by/4.0/>).

1. Introduction

Zr alloys are used as the cladding and structural components of nuclear reactor cores due to their low average neutron absorption

* Corresponding author.

E-mail address: allan.harte@manchester.ac.uk (A. Harte).

cross section and their retention of mechanical properties and corrosion resistance at operating temperatures [1]. Of the common alloying elements in the Zircaloy family of alloys, Fe, Cr and Ni, the light transition elements, are of low solubility in the α -Zr matrix [2–4] and precipitate as thermodynamically stable second phase particles (SPPs) in both the matrix and at grain boundaries [5–8]. The Sn remains homogenous in solid solution at low concentrations and acts as an α -stabiliser such that supersaturated solid solutions of Zr-6.5Sn (at.%) are stable up to 953 °C as α -phase [9]. Alloy corrosion behaviour and the resulting hydrogen ingress depends on the type and morphology of SPPs [10,11]. Better corrosion resistance has been correlated to reduced irradiation-induced growth strain [11]. SPPs and other chemical effects are known to play a role in the type, density and spatial relationship of dislocations that form as a result of irradiation [12–15].

SPPs in the Zircaloys are known to undergo irradiation-induced dissolution processes at intermediate to high neutron irradiation temperatures (280–450 °C), depleting preferentially in Fe but also in Cr and Ni in the $\text{Zr}(\text{Fe,Cr})_2$ and $\text{Zr}_2(\text{Fe,Ni})$ SPPs, respectively [6,11,16–23]. It is therefore important to study the results of this dissolution and what it means for the microstructure-related performance properties. During irradiation the Zr matrix becomes increasingly saturated in solute elements and has been shown to precipitate new Fe–, Cr– and Ni-rich phases, extending throughout the matrix with a rod-like morphology [17,24] and in higher concentration close to partially dissolved SPPs [25] compared to other parts of the matrix. Binary Zr–Fe phases, most notably Zr_3Fe , have been reported to nucleate during irradiation under PWR conditions in Zircaloy-4 [26] and under BWR conditions in Zircaloy-2 [27]. Such phases are thought to be relatively resistant to neutron irradiation at ~315–350 °C [26,28]. More recently, smaller clusters have been observed in high number density in Zircaloy-2, neutron-irradiated in a BWR to high fluences of $16.5 \times 10^{25} \text{ n m}^{-2}$ –27.5 dpa [29], and the growth of small Fe, Cr clusters has been suggested as dependent on the presence of Zr vacancies [30]. These small clusters or rods are likely to have significant effect on not only the ongoing radiation damage accumulation but also on mechanical properties such as irradiation-induced hardening [31,32].

As an analogue to neutron irradiation, we aim to assess the irradiation-induced precipitation in Zircaloy-2 after exposure to low dose proton irradiation. Proton [13,15,33,34] and ion irradiations [13,33,35,36] have been used successfully to nucleate characteristic a- and c-component dislocation loops in Zr alloys. We have recently demonstrated the similarity in the chemical evolution of pre-existing secondary phases under neutron and proton irradiation in both low-Sn ZIRLO™ [37] and Zircaloy-2 [38]. In the present work, we observe nanoprecipitation in the matrix of Zircaloy-2 and use high resolution correlative techniques for its characterisation. For the first time we use correlative atom probe tomography and scanning transmission electron microscopy with significant energy-dispersive X-ray spectroscopy capability to investigate both the compositional and crystallographic properties of the precipitates.

2. Experimental

2.1. Material

Fully recrystallised Zircaloy-2 plate was provided by Westinghouse Electric Company with nominal composition Zr-1.5Sn-0.14Fe-0.1Cr-0.06Ni (wt.%) [1], an equiaxed grain size in the range ~5–15 μm diameter and a strong basal texture in the normal direction, split $\pm 30^\circ$ in the transverse direction. The plate was cut into bars of dimensions $2 \times 2 \times 20 \text{ mm}$ and mechanically polished from the normal direction to a quality suitable for electron

backscatter diffraction, such that the grains were visible by polarised light microscopy. The bars were then proton-irradiated in the normal direction at the Michigan Ion Beam Laboratory's Tandemtron accelerator facility at 2 MeV and $350 \pm 9^\circ\text{C}$ and a current of $\sim 0.2 \mu\text{A mm}^{-2}$ for a total of 96 h. The proton irradiation dose in displacements per atom (dpa) was calculated in the Stopping Range of Ions in Matter (SRIM) utility by the quick Kinchin-Pease calculation as recommended by Stoller et al. [39] in pure, amorphous Zr with a displacement energy (E_d) of 40 eV [40]. The calculated dose level as a function of proton penetration depth is shown in Fig. 1, in which three depths are highlighted; 0.5 μm at which depth the atom probe tomography (APT) needles were extracted, 12 μm at which depth the electropolished foils were prepared for transmission electron microscopy (TEM) analysis, and 29 μm , the Bragg peak. As such, the APT data is obtained from material after ~1.5 dpa at a damage rate $\sim 4.3 \times 10^{-6} \text{ dpa s}^{-1}$ and the TEM analysis after ~2.3 dpa and $\sim 6.7 \times 10^{-6} \text{ dpa s}^{-1}$. For the control case, the non-irradiated material was used. There is a case for arguing that control material should be subject to the same temperature at time as the irradiated material. However, we deem the use of the non-irradiated baseline material as sufficient because this had been subject to full recrystallization at $> 600^\circ\text{C}$, and the irradiation temperature was much lower than this at 350 °C.

2.2. Analysis

For APT analysis, both irradiated and non-irradiated samples were mounted on arrays of silicon micro tips and annular milled with a gallium focused ion beam to obtain sharp needles with an end radius of ~50 nm. This was accomplished by milling with successively smaller annular patterns and successively lower gallium ion currents on a dual beam FEI Nova Nanolab 600 at The University of Manchester. The samples were then loaded into the Cameca Local Electrode Atom Probe (LEAP) 3000X HR at The University of Oxford, and were held at a temperature of 50 K during data acquisition. The field evaporation of ions was carried out in laser pulse mode with a green laser of energy 0.4 nJ and a frequency of 200 kHz. The reconstruction of the analysed volumes was using the commercial software IVAS 3.6.8, calibrated on the basis of the needle profile from the SEM images of the sharpened needles using IVAS software.

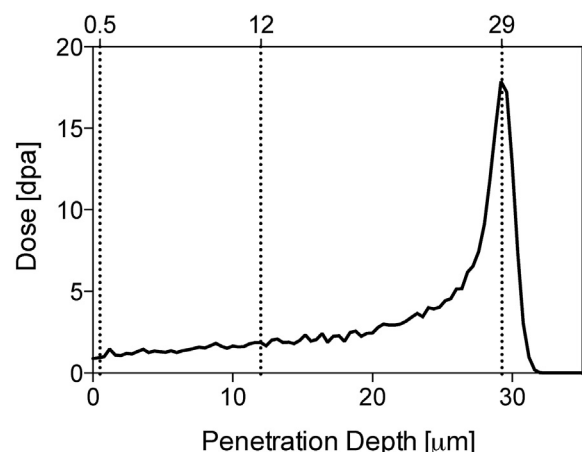


Fig. 1. Damage profile in displacements per atom (dpa) for a pure, amorphous Zr matrix with the atomic density of pure, hcp α -Zr, calculated by SRIM with the quick Kinchin-Pease option ($E_d(\text{Zr}) = 40 \text{ eV}$) and adjusted for 96 h 2 MeV proton irradiation at $\sim 0.2 \mu\text{A mm}^{-2}$. The electropolished TEM foils were prepared at a depth of ~12 μm (2.3 dpa), and the APT needles were prepared from the surface by FIB, resulting in a depth of ~0.5 μm (1.5 dpa).

For TEM analysis, electropolished foils were prepared for examination by grinding from the non-irradiated face to a thickness of $\sim 160\ \mu\text{m}$ and then electropolishing using a twin-jet Tenupol-5 electropolisher together with a Julabo FP50 cooling unit. An electrolyte of 10% perchloric acid and 20% 2-butoxyethanol in ethanol [13] was used to electropolish $\sim 12\text{--}15\ \mu\text{m}$ from both the irradiated and non-irradiated faces, the depth measured with a Keyence X200K 3D laser microscope. Subsequently, Elektron Technology's acid-resistant Lacomit varnish was used to protect the irradiated face while electropolishing to perforation from the non-irradiated face. The non-irradiated bulk material was prepared by the same method. All microscopy presented here was performed on a G2 80–200 kV spherical aberration-corrected (single, probe) FEI Titan microscope operating at 200 kV in scanning mode with a current of 0.6 nA. The microscope is equipped with a high brightness X-FEG source and the FEI ChemiSTEM™ system, comprising four energy-dispersive X-ray (EDX) detectors in close proximity to the sample, resulting in a total collection angle of 0.7 sr. While the sample was loaded in a low-background double-tilt holder, the determination of chemistry may be considered to be semi-quantitative as the Cliff-Lorimer approach was used with calculated K-factors, assuming no absorption and not accounting for Fe-scattering from the pole piece. All chemical data was obtained by spectral imaging (a full spectrum up to 20 keV at every pixel), after which chemical maps were extracted for the relevant alloying elements. Foil thickness measurements were made by an assessment of intensity oscillations in convergent beam electron diffraction (CBED) patterns by way of the graphical method [41]. Error in thickness measurements are therefore assumed to be $\pm 10\%$, given that great care was taken to obtain CBED patterns from the exact Bragg condition.

In the post-experiment analysis of the APT reconstruction we determined the dimensions of the rod-like features as follows. The rod-matrix interface was assumed to be the position at which the Fe concentration is equal to that of the average between rod-maximum and the matrix. For this calculation, 1D concentration profiles were generated across length and width dimensions of the rods, respectively. This was achieved by defining cylindrical regions of interest (ROIs), oriented in the respective analysis directions, of dimensions defined by a length exceeding that of the rod and a constant diameter of 3 nm. The 1D concentration profiles were consistently binned with 500 ions per sample and 200 ions per step. The composition of the rods was calculated by defining a ROI wholly contained within each respective rod, defined as a cylinder with a constant diameter of 2 nm and a reduced length to avoid the edge of the rod where the concentration is skewed due to the interfacial region with the matrix. This procedure limits edge effects when calculating concentrations. The detection of Ni was not carried out due to the overlapping of Ni^+ peaks with Sn^{2+} peaks at 58 and 60 Da and the Ni^{2+} peak with Zr^{3+} peak at 30 Da, leaving only 29 Da for detection of Ni, proving difficult with the low concentration of Ni (Da = mass to charge ratio). Further, Ni appears in both +1 and +2 charge states and we cannot accurately predict their field-dependent abundance. The spatial resolution of Sn in the reconstruction was limited significantly due to laser-induced surface diffusion effects as evidenced by segregation along crystallographic poles of the Zr matrix in the final APT reconstructions [29].

To obtain the dimensions of the rod-like features by STEM, spectral imaging and the resulting Fe maps from the $\langle 0001 \rangle$ direction provided good contrast against the defective α -Zr matrix and was used to obtain detailed rod width information. BF STEM imaging from the $\langle 11\bar{2}0 \rangle$ matrix orientation gave the best contrast for rod length as opposed to the Fe or Cr EDX signal, which is weak from this orientation, in which the rods are side-on and at their thinnest in the transmission direction. For quantification of number density, four images were obtained in BF STEM from the $\langle 0001 \rangle$

matrix orientation of a single grain. The determination of matrix orientation was performed by indexing the Fast Fourier Transform (FFT) of a high resolution STEM image.

The matrix orientation of a single needle was determined prior to APT by electron diffraction in a FEI Tecnai F30 FEG-TEM at the University of Manchester. This needle was mounted on a single stub so that it could be used in an on-axis TEM tomographic sample holder and mounted directly into the APT. Electron diffraction in the TEM was performed by use of the ASTAR automated crystal orientation mapping system [42], coupled with precession [43] at 0.8° at a rate of 100 Hz using the NanoMEGAS precession system to reduce dynamical effects. Precession typically increases the number of spots and improves the reliability of solutions [44] when indexed by comparison to simulated kinematical diffraction patterns in the ASTAR Index software V1.4. A probe diameter of $\sim 3\ \text{nm}$ was formed in TEM mode by using a $20\ \mu\text{m}$ diameter condenser C2 aperture and a small spot size, resulting in a low beam current of $\sim 26\ \text{pA}$. The diffraction patterns were recorded as a function of position and indexed according to phase and orientation. Two orientations were indexed normal to the needle axis and the cross-product of the two orientations was calculated to find the crystallographic orientation of the needle axis. In the APT data we then have knowledge of the reconstruction axis but not its full 3D orientation.

3. Results

The defect structures after proton irradiation to nominally 2.3 dpa involve two distinct defect types that can be observed from or close to the $\langle 11\bar{2}0 \rangle$ matrix orientation. Fig. 2 shows BF-STEM micrographs of the defect types, both of which have some degree of alignment in the $\langle 0001 \rangle$ basal plane. Neither type of defect was observed in non-irradiated material. Type I defects are elliptical loops with their long axis (10–20 nm) parallel to the $\langle 0001 \rangle$ direction and their short axis (5–10 nm) in the $\langle 0001 \rangle$ plane. Type II defects are linear defects with a short width 2–3 nm (Fig. 2a and b), are of relatively sharp contrast and, from this $\langle 11\bar{2}0 \rangle$ matrix orientation, either have their long axis parallel to the $\langle 0001 \rangle$ direction or inclined to it by an angle between 12° and 15° (Fig. 2b). Type II defects are distinct from the Type I in that they are visible when imaged parallel to the $\mathbf{g} = 0002$ systematic row (Fig. 2b), which the dislocation loops are not. This implies that the Type I defects are dislocation loops with a purely $\langle a \rangle$ -component Burgers vector and we assess these loops in detail elsewhere [15]. The nature of the Type II defects will be the focus of the remainder of this work.

From the analysis of four representative BF STEM images from the $\langle 11\bar{2}0 \rangle$ matrix orientation, it is estimated that $\sim 30\%$ of the Type II defects have their long axis parallel to $\langle 0001 \rangle$ and $\sim 70\%$ are inclined to the $\langle 0001 \rangle$ axis. However, when imaged from the $\langle 10\bar{1}0 \rangle$ orientation all Type II defects seem parallel to the $\langle 0001 \rangle$. Further, in BF STEM it was observed those of shorter lengths ($< \sim 20\ \text{nm}$) have their length parallel to $\langle 0001 \rangle$ whereas those with longer lengths tended to be inclined to $\langle 0001 \rangle$. Therefore, it is likely the case that all rods are tilted with respect to $\langle 0001 \rangle$ and the shorter, parallel rods are tilted in a symmetric orientation but appear parallel due to issues of projection. Fig. 2c and d, demonstrate that Type II defects may be imaged end-on from the $\langle 0001 \rangle$ direction. The defects highlighted in Fig. 2c and d are projected as circles or ellipses, suggesting that the Type II defects are rods and not platelets. Therefore, due to their morphology, the Type II defects will be referred to as rods hereafter. From the $\langle 0001 \rangle$ orientation, the number density of rods was calculated as $7.01 \pm 0.77 \times 10^{21}\ \text{m}^{-3}$, with the error given being a single standard deviation from the mean number of defects counted between four different images

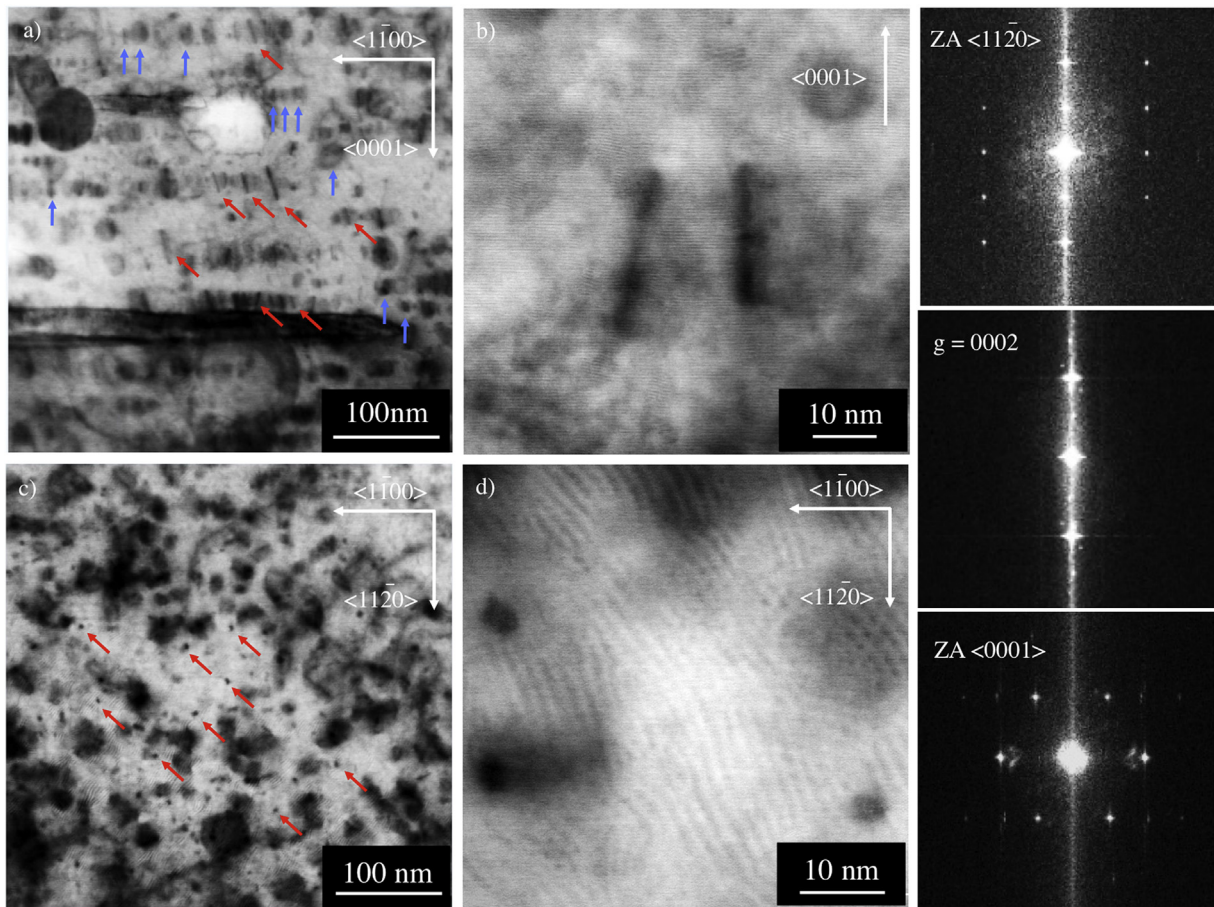


Fig. 2. BF STEM micrographs from a) the $\langle 11\bar{2}0 \rangle$ zone axis, b) between the $\langle 11\bar{2}0 \rangle$ and $\langle 10\bar{1}0 \rangle$ zone axes parallel to the $g = 0002$ systematic row, and c) and d) from the $\langle 0001 \rangle$ zone axis. FFTs of HRSTEM images to the right give the relevant orientations. Rods are highlighted in a) and c) by red tilted arrows. Dislocation loops are highlighted in a) by blue vertical arrows. (For interpretation of the references to colour in this figure legend, the reader is referred to the Web version of this article.)

within the same grain, resulting in a count of 422 defects. If we assume that rods are observed edge-on from the $\langle 11\bar{2}0 \rangle$ orientation, a defect tilted 12° from $\langle 0001 \rangle$ will have its long axis in the $\langle 1\bar{1}05 \rangle$ direction and a defect tilted 15° in the $\langle 1\bar{1}04 \rangle$.

A chemical analysis by STEM energy-dispersive X-ray spectroscopy (EDX) is given in Fig. 3, demonstrating chemical segregation to the defects displayed in Fig. 2b and d. Comparing Fig. 3a–c from the $\langle 11\bar{2}0 \rangle$ orientation with Fig. 3d–f from the $\langle 0001 \rangle$ orientation immediately demonstrates the rod morphology. However, some rods are circular in cross section (Fig. 3d bottom right) and some appear elliptical in cross section (Fig. 3d top left and bottom left). Of the 33 rods studied by EDX from the $\langle 0001 \rangle$ orientation, 19 were circular and 14 elliptical. Of the 14 elliptical, 12 were elongated along the $1\bar{1}00$ direction, consistent with the rod long axis in either the $1\bar{1}04$ or $1\bar{1}05$, 2 anomalies along $11\bar{2}0$ and zero along any direction in between. All rods observed from the $\langle 0001 \rangle$ orientation were rich in Fe and Cr but not Ni. From the $11\bar{2}0$ orientation, some Ni segregation was observed (Fig. 3c), but this was uncommon.

The rod-like morphology of the precipitates was investigated by atom probe tomography (APT), an example of which is shown in Fig. 4, where Fe and Cr enriched regions are shown by iso-concentration surfaces for the volumes with $\text{Fe} + \text{Cr} > 1.2 \text{ at.}\%$. Fig. 4a is rotated around the long needle axis by 90° to produce Fig. 4b in order to demonstrate their common direction. A total of 5 APT needles were analysed from non-irradiated Zircaloy-2 and a total of 7 needles for the proton-irradiated Zircaloy-2. Of the 5 non-irradiated needles analysed, no rods were observed. All 7 irradiated

APT needles analysed contained rods with their long axis in a common direction, such as those in Fig. 4. All rods were enriched with both Fe and Cr.

To assess whether the observed rods in APT are the same as those that we observe in the TEM, we conducted a study to determine the common orientation of the rods in the APT needles by performing both TEM diffraction analysis and APT on the same needle. In Fig. 5a and b we show the precession selected area diffraction patterns (pSADPs) from TEM with BF-TEM image inserts. In Fig. 5c and d we show the automatic indexing of those patterns on the stereographic triangle and in Fig. 5e we plot these orientations on a Kikuchi map. Fig. 5f displays the APT Fe data for that same needle, in which two rods were found at an angle $\sim 20^\circ$ to the needle axis. In Fig. 5a the needle is rotated about the needle axis by 8° relative to that in Fig. 5b. In Fig. 5c and d the precession selected area diffraction patterns are indexed as the $\langle 1\bar{5} \ 3 \ 12 \ \bar{6} \rangle$ and the $\langle 1\bar{1} \ 1 \ 10 \ \bar{3} \rangle$ for the diffraction patterns in Fig. 5a and b, respectively. The angle between two vectors in a hcp system may be calculated after Frank [45], and, indeed, the angle between these two indexed orientations is 7.6° . The cross product of two vectors gives their mutual perpendicular vector. The Miller-Bravais indices were converted to Miller indices, the cross product obtained and then converted back to Miller-Bravais to give the needle axis orientation $\langle 11 \ 1\bar{3} \ 2 \ 1\bar{8} \rangle$. The angle between this vector and the unique $\langle 0001 \rangle$ direction is 36.1° . The Kikuchi map in Fig. 5d demonstrates a way to confirm that this is correct; the common plane that connects the two orientations (dotted in orange) is the plane of the needle cross

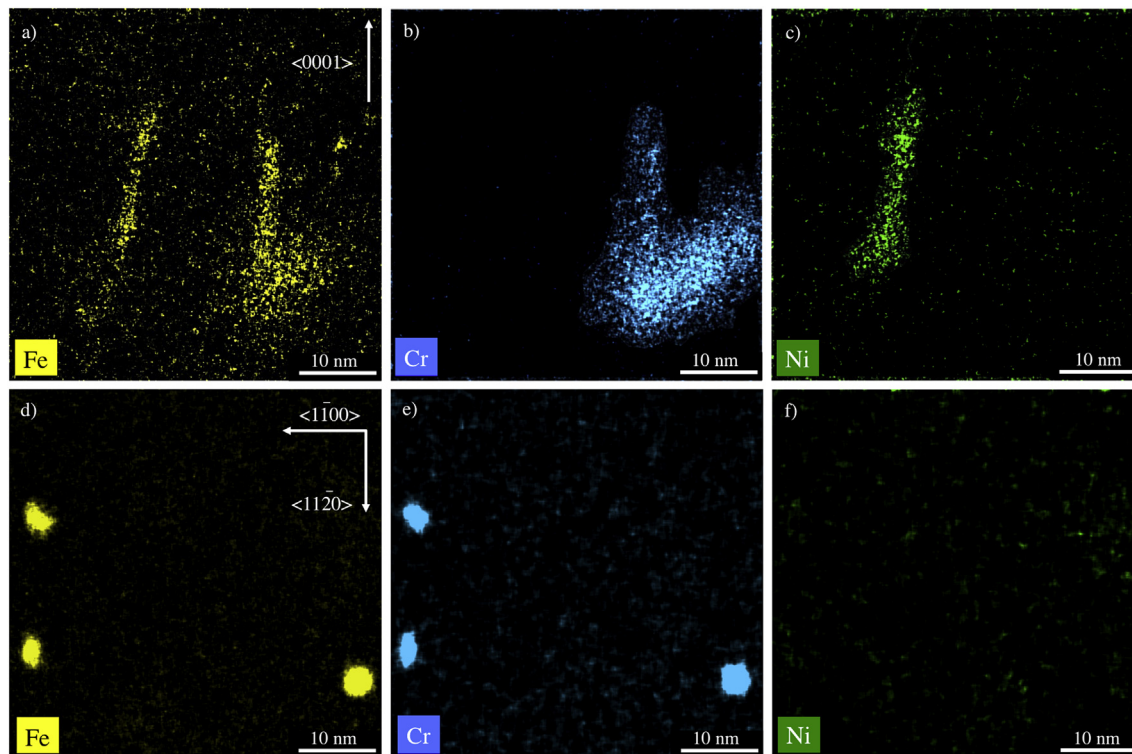


Fig. 3. Qualitative chemical Fe, Cr and Ni maps by STEM-EDX from the a)–c) $\langle 11\bar{2}0 \rangle$ orientation relating to the BF STEM image in Fig. 2b, and d)–f) from the $\langle 0001 \rangle$ orientation relating to Fig. 2d.

section and the angle of this plane with the $\langle 1\bar{2}10 \rangle$ plane gives the angle of the needle cross-section with the $\langle 0001 \rangle$ orientation; 54.4° . The needle axis is therefore $90 - 54.4 = 35.6^\circ$ from the $\langle 0001 \rangle$ orientation, a value that is very similar to the 36.1° obtained from the cross-product method. While we do not know the rotation of the APT needle around its axis with respect to the orientation at which the diffraction data was collected, the rods in Fig. 4c are $\sim 20^\circ$ from the needle axis and therefore, at a minimum, their long axis is $36 - 20 = 16^\circ$ from the $\langle 0001 \rangle$ Zr matrix orientation, which is consistent with the $12\text{--}15^\circ$ inclination measured by TEM from the $\langle 11\bar{2}0 \rangle$ matrix orientation, Fig. 2.

The distribution in rod diameter and length has been determined by both APT and STEM techniques. The data are displayed as number frequency histograms in Fig. 6, which show good agreement between the two techniques considering the small sample size. The reader is reminded that, due to the different depths that the samples were taken from, the two techniques correspond to slightly different dose levels of 1.5 and 2.3 dpa for APT (red) and BF STEM (grey), respectively. APT dimension measurements have shown no correlation between rod diameter and length. The rod diameter (Fig. 6a) ranges 2–5 nm with the modal diameter at 3 nm. Both the APT and BF STEM data give rod lengths in the range $\sim 5\text{--}30$ nm, with APT more suitable for detecting rods in the lower end of this range. The APT lengths are slightly skewed towards a modal value of 12 nm, whereas the BF STEM data gives a wider range of 15–20 nm.

Chemical analysis of the rods has been performed by both STEM-EDX and APT. For STEM-EDX, the α -Zr matrix was orientated in the $\langle 0001 \rangle$ direction to observe the rods in their most concentrated form in the transmission direction and hence minimising Zr signal from the matrix. However, the matrix contribution remains large and so the atomic per cent (at.%) of Fe and Cr within the rods remain low at < 4 at.%. The Fe/Cr ratio is thought of as reliable due

to the low solubility of the light transition elements in the α -Zr matrix [2–4]. The variation between 33 different rod compositions is displayed in Fig. 7, where chemical data is plotted against rod diameter. The compositions are quantified in at.% Fe and Cr even though there is a large contribution from the Zr matrix and pole piece scattering effects are not taken into account. The data show that rods of ~ 3 nm in diameter have higher Fe concentrations, which may suggest that these are the longest in the $\langle 0001 \rangle$ transmission direction and hence are most stable when 3 nm in diameter. While this is supported by the modal diameter of rods as 3 nm (Fig. 6a), APT measurements have shown no correlation between diameter and length. As the thickness of the TEM foil in the $\langle 0001 \rangle$ direction is known and the mean rod length determined from the $\langle 11\bar{2}0 \rangle$ orientation is also known (~ 17 nm), we may estimate the stoichiometry of the rods at $\text{Zr}_3(\text{Fe}_{0.7}\text{Cr}_{0.3})$, although the Zr contribution is difficult to be certain of.

Fig. 8a shows the distribution in the Fe/Cr atomic ratio as determined by both APT (red) and by STEM-EDX from the $\langle 0001 \rangle$ matrix orientation (grey patterned, averaged over the entire rod), which are directly comparable under the assumption that the concentration of Fe and Cr in the matrix is 0 at.% and so do not affect the STEM-EDX results. There is some agreement in the modal value between the two techniques, but APT gives a smaller range at Fe/Cr $\sim 1\text{--}2.5$ with a modal value of 2 compared to Fe/Cr $\sim 1\text{--}6.5$ and STEM-EDX gives a modal value of 2–3. Fig. 8b shows the distribution of the APT-determined atomic ratios $\text{Zr}/(\text{Fe} + \text{Cr})$ (grey open circles) and Fe/Cr (red closed circles). This demonstrates that larger rods $> \sim 400$ nm³ have lower Zr content. Considering both Fig. 8a and b, it may be concluded that the average rod has a Fe/Cr = 2 and $\text{Zr}/(\text{Fe} + \text{Cr}) = 4$. The mean composition of the rods as determined by APT at ~ 1.5 dpa is $\text{Zr}_4(\text{Fe}_{0.67}\text{Cr}_{0.33})$, tending towards $\text{Zr}_{3.1}(\text{Fe}_{0.67}\text{Cr}_{0.33})$ for rods of volume $> \sim 400$ nm³. Also included in Fig. 8b are the compositions of two Zr–Fe–Cr second phase

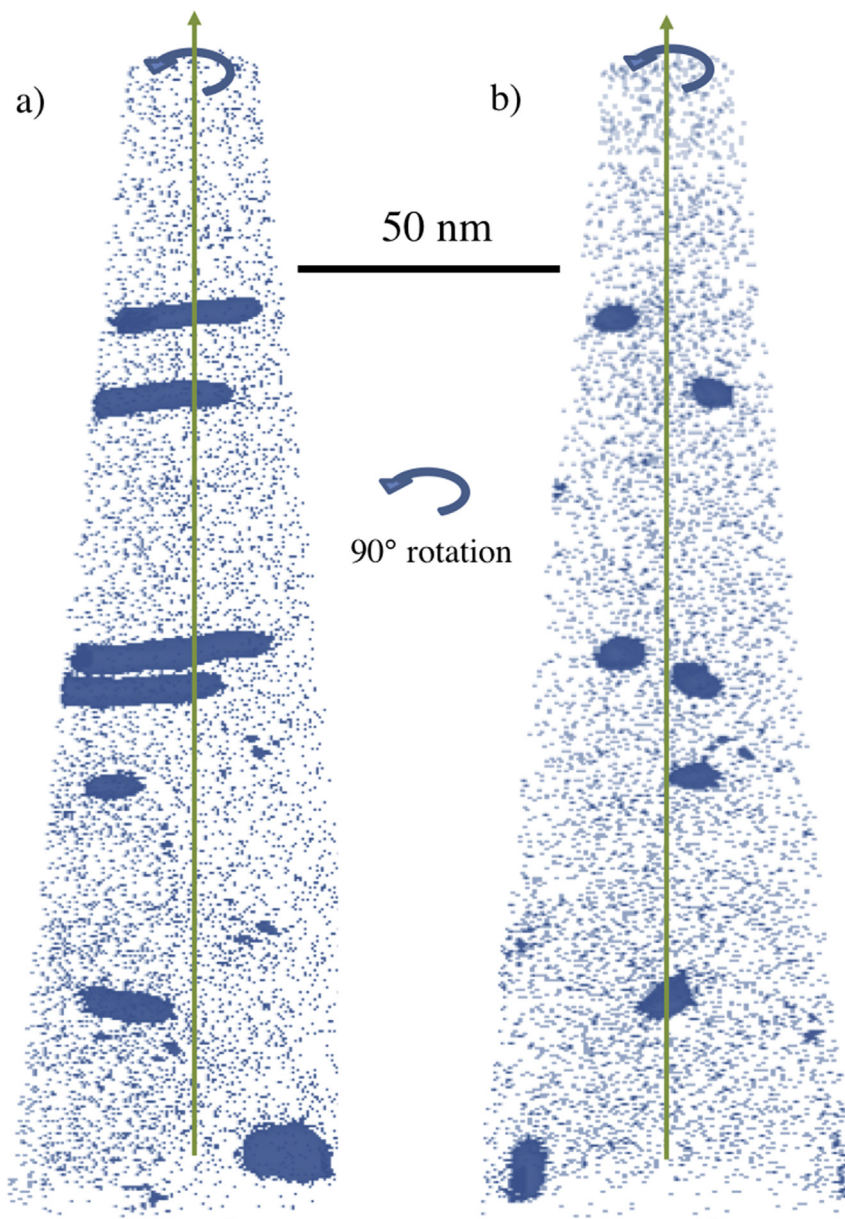


Fig. 4. APT reconstruction showing the Fe + Cr iso-concentration surface (blue, > 1.2 at.% shown only for visual clarity and perspective) rotated 90° to observe the irradiation-induced precipitates a) edge-on and b) end-on, demonstrating the rod-like morphology of the precipitates. (For interpretation of the references to colour in this figure legend, the reader is referred to the Web version of this article.)

particles (SPPs, size unknown due to intersection with edge of the reconstruction) observed by APT in non-irradiated Zircaloy-2 with compositions $\text{Zr}_{1.2}(\text{Fe}_{0.47}\text{Cr}_{0.53})_2$ and $\text{Zr}_{1.1}(\text{Fe}_{0.49}\text{Cr}_{0.51})_2$. Therefore, the non-irradiated SPPs are of a significantly different composition compared to the irradiation-induced rod precipitates.

In using STEM-EDX, it is possible to consider the rod composition in relation to the closest second phase particle (SPP). In Fig. 9 we show a cluster of SPPs consisting of one Fe–Ni SPP and two Fe–Cr. The vertical blue arrows indicate a-loops and the tilted red arrows indicate irradiation-induced rod precipitates. A qualitative example is given in Fig. 9, which shows chemical maps from the $1\bar{1}00$ matrix orientation. At the $1\bar{1}00$ matrix orientation the rods are inclined directly out of the plane of the image ($1\bar{1}04$ or $1\bar{1}05$), and, at this orientation, all rods appear to have their long axis parallel to $\langle 0001 \rangle$. This highlights the importance of analysis from multiple orientations in the TEM, an issue avoided in APT. It is clear

from Fig. 9 that the rods align with one another in the basal plane. While this was a common observation in the TEM samples, the APT samples revealed no such alignment. In Fig. 9, the rods with the highest BF contrast and the greatest EDX signal arising from Fe + Cr are the rods that are closest to the dissolving SPP; those at the top of figure are relatively weak in contrast.

The chemical composition of the 33 rods quantified by STEM-EDX from the matrix $\langle 0001 \rangle$ orientation in Figs. 6a and 7 were binned into 50 nm wide annular segments from the nearest Fe–Cr type pre-existing SPP. The results are displayed in Fig. 10, where data points are the average rod composition in that radial distance bin, i.e. in bins of 50 nm up to a maximum distance of 300 nm. Note that foil thickness is assumed to vary little within this region. While the errors from single standard deviations are significant, it can be seen that both the Fe and Cr content of rods decrease with increasing distance from the closest Fe–Cr SPP. It can also be seen

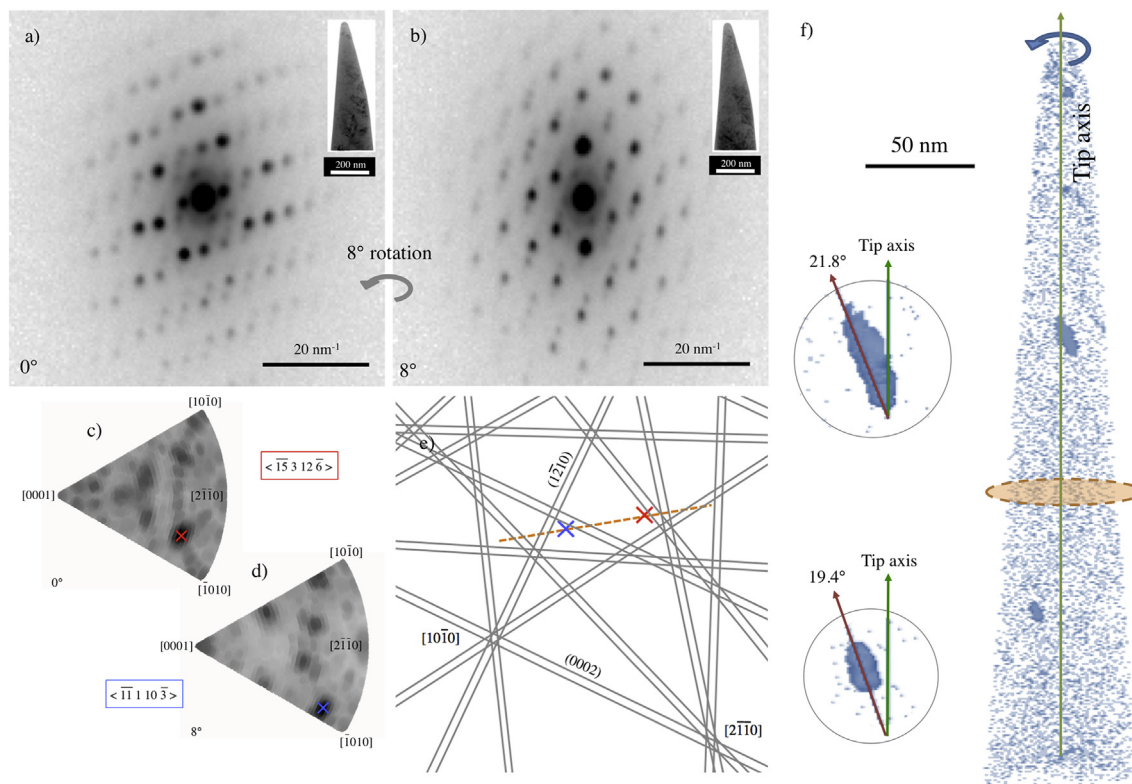


Fig. 5. Determination of rod long axis direction with respect to the Zr matrix by correlative precession selected area diffraction (pSAD) and APT. Parts a) and b) show pSADs at two rotations perpendicular to the needle axis. Parts c) and d) show the automatic indexing of those orientations on the stereographic triangle, and part e) on a Kikuchi map with their common plane dotted in orange. Part f) shows the same APT needle in Fe + Cr iso-concentration surface (>1.2 at.%) and the dotted orange cross sectional plane. (For interpretation of the references to colour in this figure legend, the reader is referred to the Web version of this article.)

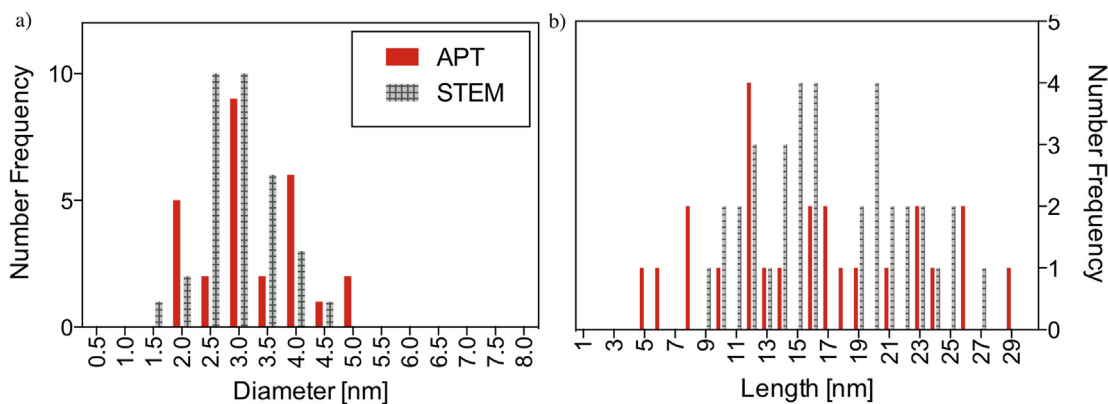


Fig. 6. The distribution in rod a) diameter and b) length have been determined by APT (red) and BF STEM from the $\langle 11\bar{2}0 \rangle$ matrix orientation (grey patterned). All APT and STEM data is plotted within the same bins, clustered around the central value of the bin. (For interpretation of the references to colour in this figure legend, the reader is referred to the Web version of this article.)

that the Cr concentration decreases more rapidly than Fe with respect to radial distance after a radius 200 nm, causing the Fe/Cr atomic ratio to increase sharply at this distance.

Matrix compositions were calculated from APT data in both irradiated and non-irradiated samples with Region of Interest (ROI) volumes containing no segregations or clusters of atoms. For this calculation, ~20 million ions were used in the non-irradiated case from two tips and ~30 million ions in the proton-irradiated case from five tips. Background subtraction was performed to obtain suitable noise reduction in two ways using different versions of the IVAS software; the first used a basic global background algorithm

and the second took neighbouring peak intensities into account. This second method did not appreciably change the values obtained. The composition of Fe was based on the 27, 28 and 28 Da peaks, for which there is overlap with the CO peak at 28 Da. This artefact was avoided by taking ROI cylinders contained within the tip volume at least 20 nm away from any surface. We find that in the non-irradiated condition the matrix contains 133 appm (81 wppm) Fe \pm 15% (standard deviation between ROI regions relative to the mean) and 187 appm (107 wppm) Cr \pm 2.2%. These values are larger than that suggested after APT measurements by Sundell; 15 wppm Fe and “virtually no Cr” [46]. However, the Fe content is

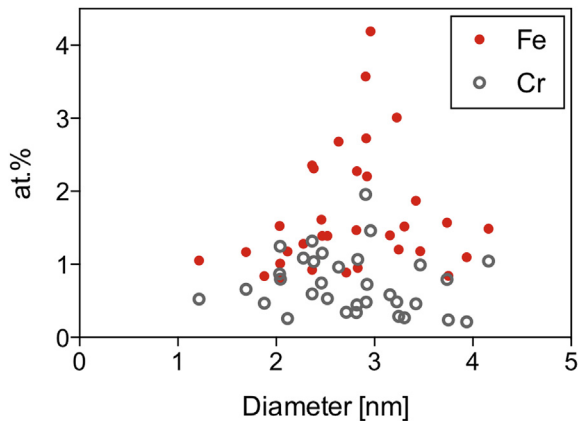


Fig. 7. STEM-EDX determination of rod composition from the (0001) α -Zr orientation as a function of rod diameter.

consistent with that suggested by Hutchinson et al.; 47–75 wppm Fe [47]. In the irradiated condition the matrix contains 140 appm (86 wppm) Fe \pm 92% and 463 (267 wppm) \pm 100% Cr. Whilst both Fe and Cr matrix content increases after irradiation, this is true for Cr much more so than Fe and there is much greater variability in measurement after irradiation. We are not aware of any post-irradiation measurement of Fe or Cr matrix content in the literature for comparison to these values, although the higher Cr content relative to Fe makes sense based on the higher Fe content relative to Cr in the rods presented here and the faster diffusivity of Fe relative to Cr in α -Zr [48].

4. Discussion

We have characterised rod-shaped structures in Zircaloy-2 plate after proton irradiation by both atom probe tomography (APT) and scanning transmission electron microscopy (STEM) coupled with

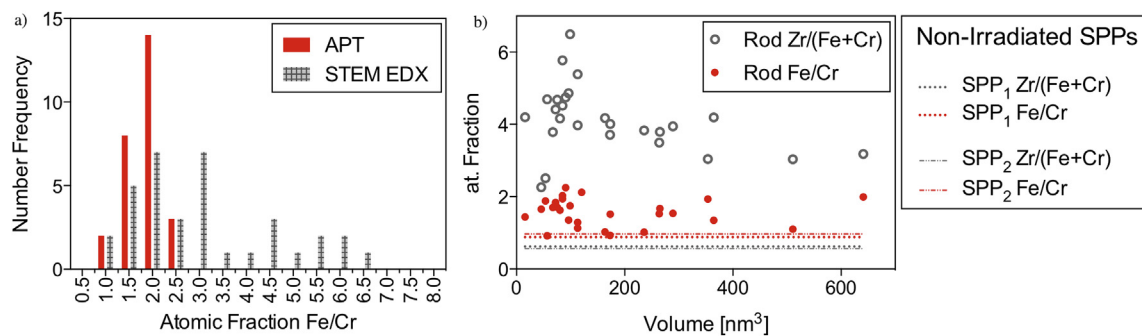


Fig. 8. A) shows a rod Fe/Cr content frequency histogram as determined by APT (red) and STEM-EDX from the (0001) matrix orientation (grey patterned). Part b) is entirely derived from APT data and shows the Fe/Cr and the Zr/(Fe + Cr) atomic fractions of both the rods and two Zr–Fe–Cr SPPs. All APT and STEM data is plotted within the same bins, clustered around the central value of the bin. (For interpretation of the references to colour in this figure legend, the reader is referred to the Web version of this article.)

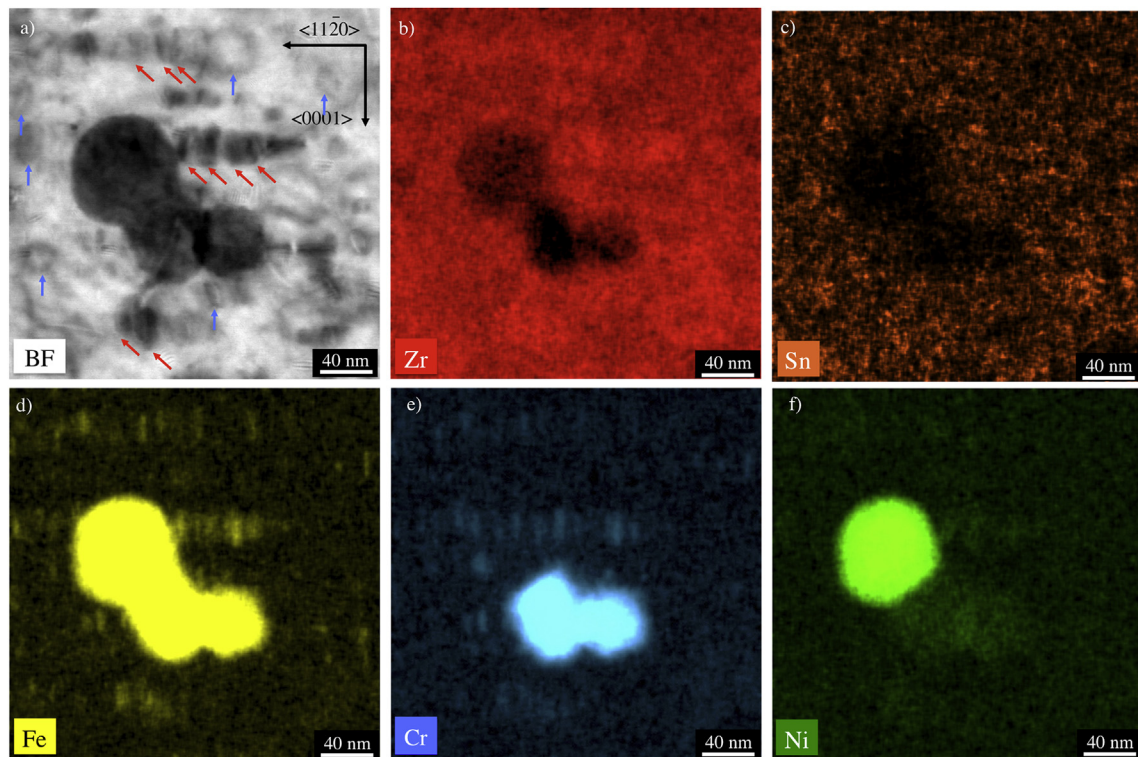


Fig. 9. Irradiation-induced rods and their chemical components are shown in close proximity to pre-existing SPPs. The BF STEM image is given in a) and the chemical maps for Zr, Sn, Fe, Cr and Ni are shown in b)–f), respectively. Rods are highlighted in a) by red tilted arrows. Dislocation loops are highlighted in a) by blue vertical arrows. (For interpretation of the references to colour in this figure legend, the reader is referred to the Web version of this article.)

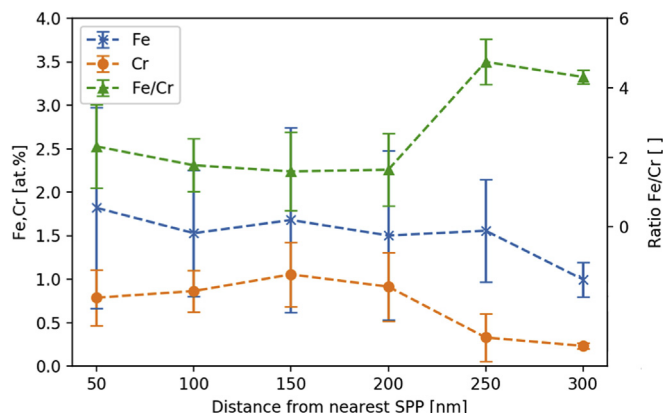


Fig. 10. The composition of rods as a function of radial distance from the closest Fe–Cr SPP are shown. The whole data set comprises the 33 rods assessed in Figs. 6a and 7, and are binned into 50 nm increments in distance from an SPP. The errors bars are a single standard deviation from the mean.

energy-dispersive X-ray (EDX) spectroscopy. In the APT data all rods within a single α -Zr grain were orientated in the same manner, as exemplified in the 90° rotation around the needle axis between Fig. 4a and b. While the uniqueness of the rod orientation may suggest that the rod long axis is in the $\langle 0001 \rangle$ direction, BF-STEM and STEM-EDX from the $\langle 11\bar{2}0 \rangle$ and $\langle 10\bar{1}0 \rangle$ matrix zone axis, Figs. 2 and 9, suggest that the rods are inclined to $\langle 0001 \rangle$ by ~ 12 – 15° . This is confirmed by correlating TEM diffraction data and APT data from the same needle, Fig. 5. However, it should be noted that the exact angle of the rod major axis with respect to the needle axis depends on the accuracy of the reconstruction. In Fig. 3c we show an inclined rod rich in Ni. Whilst this has been suggested previously [25], we did not observe this frequently, likely due to a delay in Fe–Ni type SPP dissolution relative to the Fe–Cr type SPP at this irradiation dose level [38].

Tilted dislocation loops have been observed after electron irradiation [25] with similar contrast and orientation to those shown here in Fig. 2. Very recently, proton irradiation has been shown to induce the nucleation of tilted dislocations and then the precipitation of tilted rods at those dislocations [49]. Previously, rod-shaped irradiation-induced precipitates have been observed after neutron irradiations at high fluxes, high temperatures and/or to high fluences [17,24]. Under normal power reactor conditions they have only been observed after post-irradiation annealing, resulting in the growth of such features [17]. These rods have been shown to have their long axis in $\langle 0001 \rangle$ and to align in basal planes. Power reactor fluxes result in a dose rate of $\sim 1 \times 10^{-7}$ dpa s $^{-1}$ [50,51] at $\sim 310^\circ\text{C}$ [52], and, as such, the proton irradiations here provide both a high damage rate and irradiation temperature, which seem to be necessary requirements for the nucleation of these features. It should be noted that no Sn-rich precipitates have been observed in the present work. The precipitation of Zr_5Sn_3 has been observed after neutron irradiation at high flux and temperature and has been attributed to irradiation-enhanced diffusion [17,24].

The rod dimensions demonstrated in the present work show good agreement in measurements made between APT and BF STEM or STEM-EDX mapping, Fig. 6, although the APT measurements may be skewed towards rods of shorter length due to the small analysed volume and the ignoring of larger rods that cut the APT needle surface. In regards to rod composition, it should be noted that larger scatter in measurements is expected from smaller rods as fewer ions are used in the calculation. While there does not seem to be much variation in rod composition with respect to rod volume, as determined by APT, Fig. 8b, there may be a tendency away from

$\text{Zr}_4(\text{Fe,Cr})$ and towards $\text{Zr}_3(\text{Fe,Cr})$ after rod volumes exceed 400 nm^3 (Fe/Cr ~ 2 in both cases). However, it should be noted that as smaller volumes may be more sensitive to aberrations in the APT data, which could result in more Zr content included in the composition from those small rods with a higher ratio of surface area to volume. As rods in the TEM samples may be longer than those in the APT samples, the stoichiometry estimated from STEM-EDX as $\text{Zr}_3(\text{Fe,Cr})$ (Fe/Cr ~ 2) may suggest that rods do indeed start with an atomic ratio $\text{Zr}/(\text{Fe} + \text{Cr}) \sim 4$ that tends to ~ 3 as the rods increase in size as second phase particles continue to dissolve and disperse solute into the matrix [6,16,17]. The Fe/Cr ratio has been shown to increase at distances $> \sim 200 \text{ nm}$ from the closest partially-dissolved $\text{Zr}(\text{Fe,Cr})_2$ SPP, Fig. 10, which is an indication that the rods nucleate as a result of irradiation-induced dissolute and solute redistribution, in addition to having a dependence on the relative diffusivities of Fe and Cr in the α -Zr matrix, $\text{Fe} > \text{Cr}$ [48]. Of course, due to the issue of projection in the transmission direction, there is uncertainty in that we cannot determine the distance of a rod from the SPP in the direction normal to the surface of the TEM foil. Further, SPPs located perpendicular to the foil surface polished away by sample preparation cannot be accounted for. To investigate this, we have performed an analysis of the shortest distances between SPPs in-plane in a TEM foil from Fig. 1 in Ref. [15]. Whilst SPPs can have large distances between them, they often cluster. We have found that shortest distances $< 300 \text{ nm}$ are applicable for $\sim 42\%$ of SPPs; most SPPs have a shortest inter-SPP distance of $\sim 400 \text{ nm}$, ranging 200–1000 nm. We therefore consider the data in Fig. 10 to be reliable with the caveat that distances greater than the foil thickness (150–200 nm) are less trustworthy. In further support of Fig. 10, it is indeed the case that rods rich in Fe and Cr are more frequently found close to partially-dissolved $\text{Zr}(\text{Fe,Cr})_2$ SPPs in neutron-irradiated material [25].

While the existence of the $\text{Zr}_4(\text{Fe,Cr})$ phase has been deemed ‘questionable’ by some [53], as it is not present in the Zr–Fe binary phase diagram [54,55], it has been reported in material after quenching from the α + β - or β -phase region, and is known to dissolve quickly at low fluences [6,56]. It is therefore thought to be a metastable phase and may be instrumental in the nucleation of the rods presented here. The Zr_3Fe phase, alternatively, has been reported in the literature to nucleate in Zircaloy-4-type alloys under PWR conditions [26] and in Zircaloy-2 under BWR conditions [27]. Zr–Fe phases are found in the non-irradiated state if the $\text{Fe/Cr} > 4$ (wt.%) in the total alloy composition [3], resulting in the nucleation of either Zr_3Fe or Zr_2Fe , the preference for which has been suggested depends on cooling rates [3]. The Zr_3Fe phase has been shown as stable under neutron irradiation at ~ 315 – 350°C in regards to both changes in chemistry and structure [26,28], although its amorphisation behaviour under electron irradiation is well known [57,58]. Such stability may be predicted if one considers the low melting point of the Zr_3Fe phase (885°C) in comparison to other phases, e.g. $\text{Zr}(\text{Fe,Cr})_2$ $T_{\text{melt}} = 1630^\circ\text{C}$ [59]. For a given irradiation temperature, the Zr_3Fe SPP might be better able to recover the damage incurred by thermal annealing effects in comparison to high T_{melt} SPPs. Further, the growth rate of Zr_3Fe SPPs has been shown as greater than that of $\text{Zr}(\text{Fe,Cr})_2$ in non-irradiated material during heat treatments [26] and multiple epitaxial relationships between Zr_3Fe and the α -Zr matrix have been reported [53]. Barberis et al. argued that the almost isotropic nature of the interfacial energy must mean that is not a dominating factor influencing SPP nucleation and stabilisation [53]. If the rods investigated here are indeed Zr_3Fe in structure, their morphology must be due to the preferential $\langle 0001 \rangle$ diffusional anisotropy of Fe, Cr and Ni in α -Zr [60], supported by their observation under high neutron irradiation temperatures and flux [17,24].

The rods observed in the present work are thought to be

crystalline for the following reasons, namely the alignment of the rods with the crystallography of the α -Zr matrix and with one another, and the general consistency in chemical composition, both between different rods and within individual rods, the latter investigated by the use of proximity histograms [61]. However, the rods proved too small for structural analysis by electron diffraction. In the literature, Zr_3Fe is observed with orthorhombic crystal structure with lattice parameters $a = 0.33$ nm, $b = 1.1$ nm and $c = 0.88$ nm [3].

The geometric arrangement of clusters during the early stages of precipitation has been investigated recently by Burr et al. using *ab initio* DFT calculations, which show that clusters of Fe, Cr or Fe + Cr around a Zr vacancy induce less lattice strain than that of an isolated interstitial defect [30]. The proposed necessity of a Zr vacancy defect for Fe and Cr clustering is interesting, as it helps explain the correlation between matrix solute content and vacancy c-loop nucleation [12] and the existence of a high density of vacancy c-loops in the vicinity of partially-dissolved SPPs [12–14]. The growth of clusters may be attributed to their increasing stability with increasing size; recent calculations by Varvenne et al. have shown that the binding energy, and therefore the stability, of clusters increases with n up to $n = 7$ [62] where n refers to the number of atoms/vacancies in the cluster, with the most stable configurations as 3D clusters, in agreement with earlier calculations for clusters of ≤ 10 vacancies [63,64]. Larger vacancy clusters may induce the nucleation of larger Fe, Cr clusters [30].

In the present work we find rods and not clusters, but clusters that contain predominantly Fe and Cr (Ni to a much lesser extent) have recently been detected by APT in Zircaloy-2 cladding material after irradiation in a BWR to a high fluence of 16.5×10^{25} n m^{-2} –27.5 dpa [29]. While the composition was highly variable in the 1–5 nm diameter clusters, and therefore the structure likely non-crystallographic, Sundell et al. clearly demonstrated that the clusters segregate in planar arrays separated by a distance of ~ 10 nm [29]. These planes were assumed to be basal (0001) planes due to their uniqueness, but orientation information was not available from the APT data sets. The calculations by Burr et al. demonstrate clustering predominantly in basal planes [30], which agrees with the alignment between rods in the present work and corroborates the assumed plane in the work of Sundell et al. [29] and the alignment between irradiation-induced precipitates in the basal plane reported in the literature [17,24]. The number density of clusters reported by APT in neutron-irradiated material was high at $8 \pm 2 \times 10^{23} \text{ m}^{-3}$. The number density of a-loops is given by Carpenter and Northwood at 25 dpa (a slightly lower dose than that of Sundell et al.) as $\sim 2 \times 10^{22} \text{ m}^{-3}$ [65], which indicates that the cluster number density is higher than that of a-loops by a factor of 40, although Sundell et al. suggest a factor of 10. In the present work, the density of rods is calculated to be $7.01 \pm 0.77 \times 10^{21} \text{ m}^{-3}$. According to Carpenter and Northwood, the a-loop number density at ~ 2.3 dpa should be close to $3 \times 10^{22} \text{ m}^{-3}$ for neutron irradiated Zircaloy-2 [65], which is higher than the rod density by a factor of ~ 4 . However, the a-loop number density that we have calculated for the proton-irradiated Zircaloy-2 is lower at $2.14 \pm 0.73 \times 10^{21} \text{ m}^{-3}$ [15], and, as such, the rod number density is higher than that of the a-loop number density by a factor of ~ 3 . If one considers the volume of material exhibiting clustering behaviour by Sundell et al. (assuming an average cluster sphere of diameter 3 nm) and that of the present work, combining the APT and STEM measurements, the total volume fraction of clusters in the former ($\sim 1.1 \times 10^{-3}$) is higher than that presented here ($\sim 1.2 \times 10^{-4}$) by a factor of ~ 9 . Such a difference may be related to the higher degree of SPP irradiation-induced dissolution at the higher dose studied by Sundell et al.

The high density of clusters and rods observed after irradiation is likely to have an effect on macroscopic properties. The alignment

of rods in the (0001) plane presented here is similar to the alignment of a-loops in neutron-irradiated material [66] and so we may expect significant interactions between the two structures. Chemical segregation to dislocation loops has been discussed as likely to change the loop bias for point defects and clusters, and, as a consequence, is thought to be important in the stability, shape and evolution of dislocation structures [25]. The presence of solute has been shown as influential towards c-loop density [12] and a high density of c-loops is correlated to the accelerated regime of irradiation-induced growth [67]. Further, the effect of variable solute segregation to dislocations in different alloys and at different irradiation doses has been suggested as a source of variation in both a-loop size and in irradiation-induced hardening measurements in Zircaloy-2 and -4 [22,31,32]. As dislocation loops are thought to be intrinsically related to macroscopic irradiation-induced growth strain, their interaction with dispersed solute and its clustering is worthy of further investigation.

5. Conclusions

We have investigated the nature of nano-rods that precipitate as a result of proton irradiation and have discussed their importance with regard to their neutron-irradiation analogues. We have utilised correlative analysis in APT, electron diffraction and STEM-EDX, with good agreement between the techniques in terms of rod morphology, crystallography, dimensions and composition. Small rods are observed to have composition $\text{Zr}_4(\text{Fe}_{0.67}\text{Cr}_{0.33})$, tending towards $\text{Zr}_3(\text{Fe}_{0.69}\text{Cr}_{0.31})$ as the rod volume increases to $> \sim 400 \text{ nm}^3$, and most rods are considered to have their long axis inclined to (0001) by 12 – 15° , i.e. in the $\langle 1\bar{1}04 \rangle$ or $\langle 1\bar{1}05 \rangle$ Zr matrix direction, similar to those observed in neutron irradiated material. The rod Fe/Cr atomic ratio is shown to increase at distances $> \sim 200$ nm from the closest partially-dissolved $\text{Zr}(\text{Fe,Cr})_2$ SPP, suggesting that the rods nucleate as a result of the irradiation-induced dissolution of pre-existing intermetallic phases and that their chemical composition depends on the relative diffusivities of Fe and Cr in the α -Zr matrix. At 2.3 dpa, the number density of rods is calculated to be higher than that of a-loops by a factor of ~ 3 . Therefore, the implications for macroscopic strain-related phenomena, such as irradiation-induced growth and hardening, may be significant.

Acknowledgements

This work is funded by an EPSRC Leadership Fellowship [EP/I005420/1] for the study of irradiation damage in zirconium alloys, and is supported heavily by industrial contributors and especially Westinghouse and Studsvik in terms of both material acquisition and useful discussions. The authors would like to thank Thomas Seymour for aid in experimental accomplishments and Gary Was and Ovidiu Toader at the Michigan Ion Beam Laboratory for the use of their facility in the proton irradiation experiments. The University of Oxford Atom Probe Facility acknowledges EPSRC support under EP/M022803/1.

References

- [1] L. Hallstadius, S. Johnson, E. Lahoda, Cladding for high performance fuel, Prog. Nucl. Energy 57 (2012) 71–76, <https://doi.org/10.1016/j.pnucene.2011.10.008>.
- [2] M.M. Stupel, M. Bamberger, B.Z. Weiss, Determination of Fe solubility in αZr by Mössbauer spectroscopy, Scripta Metall. 19 (1985) 739–740.
- [3] D. Charquet, R. Hahn, E. Ortlieb, J. Gros, J. Wadier, Solubility limits and formation of intermetallic precipitates in ZrSnFeCr alloys, Zircon. Nucl. Ind. Eighth Int. Symp. (1988) 405–422.
- [4] H. Zou, G.M. Hood, H. Nakajima, J.A. Roy, R.J. Schultz, The solid solubility of Ni and Co in α -Zr: a secondary ion mass spectrometry study, J. Nucl. Mater. 223

- (1995) 186–188, [https://doi.org/10.1016/0022-3115\(95\)00023-2](https://doi.org/10.1016/0022-3115(95)00023-2).
- [5] R. Kuwae, K. Sato, E. Higashinakagawa, J. Kawashima, S. Nakamura, Mechanism of Zircaloy nodular corrosion, *J. Nucl. Mater.* 119 (1983) 229–239.
- [6] W.J.S. Yang, R.P. Tucker, R.B. Adamson, Precipitates in Zircaloy: identification and the effects of irradiation and thermal treatment, *J. Nucl. Mater.* 138 (1986) 185–195.
- [7] M. Griffiths, R.W. Gilbert, V. Fidleris, R.P. Tucker, R.B. Adamson, Neutron damage in zirconium alloys irradiated at 644 to 710 K, *J. Nucl. Mater.* 150 (1987) 159–168, [https://doi.org/10.1016/0022-3115\(87\)90071-7](https://doi.org/10.1016/0022-3115(87)90071-7).
- [8] H. Zou, G.M. Hood, J.A. Roy, R.H. Packwood, V. Weatherall, Solute distribution in annealed Zircaloy-2 and Zr-2.5Nb, *J. Nucl. Mater.* 208 (1994) 159–165, [https://doi.org/10.1016/0022-3115\(94\)90207-0](https://doi.org/10.1016/0022-3115(94)90207-0).
- [9] H. Okamoto, Sn-Zr (Tin-zirconium), *J. Phase Equilibria Diffusion* 31 (2010) 411–412, <https://doi.org/10.1007/s11669-010-9734-4>.
- [10] F. Garzarolli, R. Schumann, E. Steinberg, Corrosion optimized Zircaloy for boiling water reactor (BWR) fuel elements, *Zircon, Nucl. Ind. Tenth Int. Symp. ASTM STP 1245* (1994) 709–723.
- [11] S. Valizadeh, G. Ledergerber, S. Abolhassan, D. Jädnäs, M. Dahlbäck, E.V. Mader, G. Zhou, J. Wright, L. Hallstadius, Effects of secondary phase particle dissolution on the in-reactor performance of BWR cladding, *J. ASTM Int. (JAI)* 8 (2014) 729–753, <https://doi.org/10.1520/JAI103025>.
- [12] M. Griffiths, R.W. Gilbert, The Formation of c-component defects in zirconium alloys during neutron irradiation, *J. Nucl. Mater.* 150 (1987) 169–181.
- [13] L. Tournadre, F. Onimus, J.-L. Béchade, D. Gilbon, J.-M. Cloué, J.-P. Mardon, X. Feaugas, O. Toader, C. Bachelet, Experimental study of the nucleation and growth of c-component loops under charged particle irradiations of recrystallized Zircaloy-4, *J. Nucl. Mater.* 425 (2012) 76–82, <https://doi.org/10.1016/j.jnucmat.2011.11.061>.
- [14] Y. de Carlan, C. Regnard, M. Griffiths, D. Gilbon, C. Lemaignan, Influence of iron in the nucleation of <c> component dislocation loops in irradiated Zircaloy-4, *Zircon, Nucl. Ind. Elev. Int. Symp. ASTM STP 1295* (1996) 638–653.
- [15] A. Harte, D. Jädnäs, M. Topping, P. Frankel, C. Race, J. Romero, L. Hallstadius, E.C. Darby, M. Preuss, The effect of matrix chemistry on dislocation evolution in an irradiated Zr alloy, *Acta Mater.* 130 (2017) 69–82.
- [16] R.W. Gilbert, M. Griffiths, G.J.C. Carpenter, Amorphous intermetallics in neutron irradiated Zircaloys after high fluences, *J. Nucl. Mater.* 135 (1985) 265–268.
- [17] M. Griffiths, R.W. Gilbert, G.J.C. Carpenter, Phase instability, decomposition and redistribution of intermetallic precipitates in Zircaloy-2 and -4 during neutron irradiation, *J. Nucl. Mater.* 150 (1987) 53–66, <https://doi.org/10.1159/000361068>.
- [18] W.J.S. Yang, Precipitate stability in neutron-irradiated Zircaloy-4, *J. Nucl. Mater.* 158 (1988) 71–80.
- [19] M. Griffiths, Comments on precipitate stability in neutron-irradiated Zircaloy-4, *J. Nucl. Mater.* 170 (1990) 294–300.
- [20] X. Meng, D. Northwood, Second phases in Zircaloy-2, *J. Nucl. Mater.* 168 (1989) 125–136.
- [21] Y. Etoh, S. Shimada, Neutron irradiation effects on intermetallic precipitates in Zircaloy as a function of fluence, *J. Nucl. Mater.* 200 (1993) 59–69, [https://doi.org/10.1016/0022-3115\(93\)90009-N](https://doi.org/10.1016/0022-3115(93)90009-N).
- [22] B.V. Cockeram, K.J. Leonard, L.L. Snead, M.K. Miller, The use of a laser-assisted Local Electrode Atom Probe and TEM to examine the microstructure of Zircaloy and precipitate structure following low dose neutron irradiation at nominally 358°C, *J. Nucl. Mater.* 433 (2013) 460–478, <https://doi.org/10.1016/j.jnucmat.2012.10.006>.
- [23] T. Sawabe, T. Sonoda, S. Kitajima, T. Kameyama, Analysis of atomic distribution in as-fabricated Zircaloy-2 claddings by atom probe tomography under high-energy pulsed laser, *J. Nucl. Mater.* 442 (2013) 168–174, <https://doi.org/10.1016/j.jnucmat.2013.08.048>.
- [24] O.T. Woo, G.J.C. Carpenter, Radiation-induced precipitation in Zircaloy-2, *J. Nucl. Mater.* 159 (1988) 397–404.
- [25] M. Griffiths, A review of microstructure evolution in zirconium alloys during irradiation, *J. Nucl. Mater.* 159 (1988) 190–218.
- [26] F. Garzarolli, W. Goll, A. Seibold, I. Ray, Effect of in-PWR irradiation on size, structure, and composition of intermetallic precipitates of Zr alloys, *Zircon. Nucl. Ind. Elev. Int. Symp. ASTM STP 1295* (1996) 541–556.
- [27] W. Goll, I. Ray, The behavior of intermetallic precipitates in highly irradiated BWR LTP cladding, *Zircon. Nucl. Ind. Thirteenth. Int. Symp. ASTM STP 1423* (2002) 80–95.
- [28] V.N. Shishov, A. V. Nikulina, V.A. Markelov, M.M. Peregud, A. V. Kozlov, S.A. Averin, S.A. Kolbenkov, A.E. Novoselov, Influence of neutron irradiation on dislocation structure and phase composition of Zr-Base alloys, *Zircon. Nucl. Ind. Elev. Int. Symp. ASTM STP 1295* (1996) 603–622.
- [29] G. Sundell, M. Thuvander, P. Tejlund, M. Dahlbäck, L. Hallstadius, H.-O. Andren, Redistribution of alloying elements in Zircaloy-2 after in-reactor exposure, *J. Nucl. Mater.* 454 (2014) 178–185.
- [30] P. a Burr, M.R. Wenman, B. Gault, M.P. Moody, M. Ivermark, M. Preuss, L. Edwards, R.W. Grimes, From solid solution to cluster formation of Fe and Cr in α -Zr, *J. Nucl. Mater.* 467 (2015) 320–331.
- [31] B.V. Cockeram, K.J. Leonard, T.S. Byun, L.L. Snead, J.L. Hollenbeck, Development of microstructure and irradiation hardening of Zircaloy during low dose neutron irradiation at nominally 358 C, *J. Nucl. Mater.* 418 (2011) 46–61, <https://doi.org/10.1016/j.jnucmat.2014.03.004>.
- [32] B.V. Cockeram, K.J. Leonard, T.S. Byun, L.L. Snead, J.L. Hollenbeck, Development of microstructure and irradiation hardening of Zircaloy during low dose neutron irradiation at nominally 377–440 C, *J. Nucl. Mater.* 449 (2014) 69–87, <https://doi.org/10.1016/j.jnucmat.2014.03.004>.
- [33] X.T. Zu, K. Sun, M. Atzmon, L.M. Wang, L.P. You, F.R. Wan, J.T. Busby, G.S. Was, R.B. Adamson, Effect of proton and Ne irradiation on the microstructure of Zircaloy 4, *Philos. Mag. A* 85 (2005) 649–659, <https://doi.org/10.1080/14786430412331320017>.
- [34] L. Tournadre, F. Onimus, J. Béchade, D. Gilbon, J. Cloué, J. Mardon, X. Feaugas, Toward a better understanding of the hydrogen impact on the radiation induced growth of zirconium alloys, *J. Nucl. Mater.* 441 (2013) 222–231.
- [35] Y. Idrees, Z. Yao, M.A. Kirk, M.R. Daymond, In situ study of defect accumulation in zirconium under heavy ion irradiation, *J. Nucl. Mater.* 433 (2013) 95–107, <https://doi.org/10.1016/j.jnucmat.2012.09.014>.
- [36] Y. Idrees, Z. Yao, M. Sattari, M.A. Kirk, M.R. Daymond, Irradiation-induced microstructural changes in Zr-Excel alloy, *J. Nucl. Mater.* 441 (2013) 138–151, <https://doi.org/10.1016/j.jnucmat.2013.05.036>.
- [37] E.M. Francis, A. Harte, P. Frankel, S.J. Haigh, D. Jädnäs, J. Romero, L. Hallstadius, M. Preuss, Iron redistribution in a zirconium alloy after neutron and proton irradiation studied by energy-dispersive X-ray spectroscopy (EDX) using an aberration-corrected (scanning) transmission electron microscope, *J. Nucl. Mater.* 454 (2014) 387–397.
- [38] A. Harte, M. Topping, P. Frankel, D. Jädnäs, J. Romero, L. Hallstadius, Nano-scale chemical evolution in a proton- and neutron-irradiated Zr alloy, *J. Nucl. Mater.* 487 (2017) 30–42.
- [39] R.E. Stoller, M.B. Toloczko, G.S. Was, A.G. Certain, S. Dwaraknath, F. a. Garner, On the use of SRIM for computing radiation damage exposure, *Nucl. Instrum. Meth. Phys. Res. B* 310 (2013) 75–80, <https://doi.org/10.1016/j.nimb.2013.05.008>.
- [40] G.S. Was, Fundamentals of radiation materials Science, in: *Fundam. Radiat. Mater. Sci.*, Springer Berlin Heidelberg, New York, 2007, p. 83.
- [41] D.B. Williams, C.B. Carter, 21.2 Thickness determination, in: *Transm. Electron Microsc. A Textb. Mater. Sci.*, Springer Science+Business Media, LLC, 223 Spring Street, New York, NY, 10013, USA, 2009, pp. 352–354.
- [42] E.F. Rauch, L. Dupy, Rapid spot diffraction patterns identification through template matching, *Arch. Met. Mater.* 50 (2005) 87–99.
- [43] R. Vincent, P.A. Midgley, Double conical beam-rocking system for measurement of integrated electron diffraction intensities, *Ultramicroscopy* 53 (1994) 271–282.
- [44] E.F. Rauch, M. Véron, J. Portillo, D. Bultreys, Y. Maniette, S. Nicolopoulos, Automatic crystal orientation and phase mapping in TEM by precession diffraction, *Microsc. Anal.* 22 (2008) S5–S8.
- [45] F.C. Frank, On miller–bravais indices and four-dimensional vectors, *Acta Crystallogr.* 18 (1965) 862–866, <https://doi.org/10.1107/S0365110X65002116>.
- [46] G. Sundell, Atomic Scale Degradation of Zirconium Alloys for Nuclear Applications, Chalmers University of Technology, 2015.
- [47] B. Hutchinson, B. Lehtinen, M. Limbäck, M. Dahlbäck, Study of the structure and chemistry in Zircaloy-2 and the resulting oxide after high temperature corrosion, *J. ASTM Int. (JAI)* 4 (2007).
- [48] R.A. Perez, H. Nakajima, F. Dymont, Diffusion in alpha-Ti and Zr, *Mater. Trans.* 44 (2003) 2–13.
- [49] M. Topping, A. Harte, P. Frankel, G. Sundell, M. Thuvander, H.O. Andren, D. Jädnäs, P. Tejlund, J. Romero, E.C. Darby, S. Dumbill, L. Hallstadius, M. Preuss, The effect of iron on dislocation evolution in model and commercial zirconium alloys, *Zircon. Nucl. Ind. Eighteenth Int. Symp.* (2018) 796–821, <https://doi.org/10.1520/STP159720160068>. ASTM STP1597.
- [50] V.N. Shishov, M.M. Peregud, A. V. Nikulina, G.P. Kobylansky, Z.E. Ostrovsky, Influence of structure-phase state of Nb containing Zr alloys on irradiation-induced growth, *Zircon. Nucl. Ind. 14th Symp.* 2 (2005) 666–685.
- [51] R. Adamson, Charged Particle Bombardment of Zirconium Alloys: a Review, Sweden, 2014.
- [52] C.R.F. Azevedo, Selection of fuel cladding material for nuclear fission reactors, *Eng. Fail. Anal.* 18 (2011) 1943–1962, <https://doi.org/10.1016/j.jengfailanal.2011.06.010>.
- [53] P. Barberis, N. Dupin, C. Lemaignan, A. Pasturel, J. Grange, Microstructure and phase control in Zr-Fe-Cr-Ni alloys: thermodynamic and kinetic aspects, *J. ASTM Int. (JAI)* 2 (2005) 129–156, <https://doi.org/10.1520/JAI12771>.
- [54] F. Stein, G. Sauthoff, M. Palm, Experimental determination of intermetallic phases, phase equilibria, and invariant reaction temperatures in the Fe-Zr system, *J. Phase Equil.* 23 (2002) 480–494, <https://doi.org/10.1361/105497102770331172>.
- [55] H. Okamoto, Fe-Zr (iron-zirconium), *J. Phase Equilibria Diffusion* 27 (2006) 543–544, <https://doi.org/10.1361/154770306X136601>.
- [56] B.-C. Cheng, R.M. Kruger, R.B. Adamson, Corrosion behavior of irradiated Zircaloy, *Zircon. Nucl. Ind. Tenth Int. Symp. ASTM STP 1245* (1994).
- [57] A.T. Motta, L.M. Howe, P.R. Okamoto, Amorphization kinetics of Zr3Fe under electron irradiation, *J. Nucl. Mater.* 205 (1993) 258–266.
- [58] A.T. Motta, Amorphization of intermetallic compounds under irradiation — a review, *J. Nucl. Mater.* 244 (1997) 227–250, [https://doi.org/10.1016/S0022-3115\(96\)00740-4](https://doi.org/10.1016/S0022-3115(96)00740-4).
- [59] A.T. Motta, C. Lemaignan, A ballistic mixing model for the amorphization of precipitates in Zircaloy under neutron irradiation, *J. Nucl. Mater.* 195 (1992) 277–285, [https://doi.org/10.1016/0022-3115\(92\)90519-Q](https://doi.org/10.1016/0022-3115(92)90519-Q).
- [60] M. Christensen, W. Wolf, C.M. Freeman, E. Wimmer, R.B. Adamson, L. Hallstadius, P.E. Cantonwine, E.V. Mader, Effect of alloying elements on the properties of Zr and the Zr–H system, *J. Nucl. Mater.* 445 (2014) 241–250,

- <https://doi.org/10.1016/j.jnucmat.2013.10.040>.
- [61] O.C. Hellman, J.A. Vandenbroucke, J. Rüsing, D. Isheim, D.N. Seidman, Analysis of three-dimensional atom-probe data by the proximity histogram, *Microsc. Microanal.* 6 (2000) 437–444, <https://doi.org/10.1007/s100050010051>.
- [62] C. Varvenne, O. Mackain, E. Clouet, Vacancy clustering in zirconium: an atomic-scale study, *Acta Mater.* 78 (2014) 65–77, <https://doi.org/10.1016/j.actamat.2014.06.012>.
- [63] N. de Diego, A. Serra, D.J. Bacon, Y.N. Osetsky, On the structure and mobility of point defect clusters in alpha-zirconium: a comparison for two interatomic potential models, *Model. Simulat. Mater. Sci. Eng.* 19 (2011) 35003.
- [64] D. Kulikov, M. Hou, Vacancy dislocation loops in zirconium and their interaction with self-interstitial atoms, *J. Nucl. Mater.* 342 (2005) 131–140, <https://doi.org/10.1016/j.jnucmat.2005.04.004>.
- [65] G.J.C. Carpenter, D.O. Northwood, The contribution of dislocation loops to radiation growth and creep of Zircaloy-2, *J. Nucl. Mater.* 56 (1975) 260–266.
- [66] A. Jostsons, P.M. Kelly, G.R. Blake, The nature of dislocation loops in neutron irradiated zirconium, *J. Nucl. Mater.* 66 (1977) 236–256.
- [67] R.A. Holt, R.W. Gilbert, c-component dislocations in annealed Zircaloy irradiated at about 570 K, *J. Nucl. Mater.* 137 (1986) 185–189, [https://doi.org/10.1016/0022-3115\(86\)90218-7](https://doi.org/10.1016/0022-3115(86)90218-7).